npj | Quantum Materials

www.nature.com/npjquantmats

ARTICLE OPEN

Probing the reconstructed Fermi surface of antiferromagnetic $BaFe_2As_2$ in one domain

Matthew D. Watson[1,2], Pavel Dudin[1], Luke C. Rhodes[1,2,3], Daniil V. Evtushinsky[4], Hideaki Iwasawa[1,5], Saicharan Aswartham[6], Sabine Wurmehl[6], Bernd Büchner[6,7], Moritz Hoesch[1,8] and Timur K. Kim[1]

A fundamental part of the puzzle of unconventional superconductivity in the Fe-based superconductors is the understanding of the magnetic and nematic instabilities of the parent compounds. The issues of which of these can be considered the leading instability, and whether weak- or strong-coupling approaches are applicable, are both critical and contentious. Here, we revisit the electronic structure of $BaFe_2As_2$ using angle-resolved photoemission spectroscopy (ARPES). Our high-resolution measurements of samples "detwinned" by the application of a mechanical strain reveal a highly anisotropic 3D Fermi surface in the low-temperature antiferromagnetic phase. By comparison of the observed dispersions with ab initio calculations, we argue that overall it is magnetism, rather than orbital/nematic ordering, which is the dominant effect, reconstructing the electronic structure across the Fe 3*d* bandwidth. Finally, using a state-of-the-art nano-ARPES system, we reveal how the observed electronic dispersions vary in real space as the beam spot crosses domain boundaries in an unstrained sample, enabling the measurement of ARPES data from within single antiferromagnetic domains, and showing consistence with the effective mono-domain samples obtained by detwinning.

npj Quantum Materials (2019)4:36 ; https://doi.org/10.1038/s41535-019-0174-z

INTRODUCTION

Unconventional superconductivity in the Fe-based systems emerges in proximity to antiferromagnetic (AFM) and "nematic" phases, which are both characterised by pronounced magnetic and electronic anisotropies. As the fluctuations associated with these phases are likely to be important for the superconducting pairing, the ordered phases of the parent compounds, of which $BaFe_2As_2$ is the archetype, have been the subject of intense investigations. Although in $BaFe_2As_2$ the orthorhombic structural (nematic) and magnetic transitions occur simultaneously at $T_s = T_N = 137$ K, the decoupling of the two transition temperatures in $Ba(Fe_{1-x}Co_x)_2As_2$,[1] NaFeAs,[2] and FeSe[3] has caused much debate about the relative importance of magnetic and orbital degrees of freedom.[4,5] Some theoretical studies have interpreted the nematic (non-magnetic orthorhombic) phase as still being essentially magnetically driven,[4,6] with a critical role played by significant biquadratic exchange interactions.[7,8] However, another view is that the presence of a non-magnetic symmetry-breaking transition shows that orbital degrees of freedom need to be treated on at least an equal footing.[5,9–11] It is therefore important to experimentally probe the ground state of the parent compounds, but a recurring experimental challenge is that when fourfold symmetry is spontaneously broken at T_s, the samples naturally form orthorhombic twin domains, restoring macroscopic fourfold symmetry and masking the underlying anisotropies. To address this, it was found that samples could be effectively "detwinned" by the application of a mechanical strain along the Fe–Fe direction.[12] Experiments performed on such "detwinned" samples have yielded several important breakthroughs, in particular revealing pronounced intrinsic in-plane electronic anisotropies in measurements of resistivity and optical spectroscopy,[13,14] phonon frequencies split by magnetic interactions,[15] and strongly anisotropic magnetic excitations in inelastic neutron scattering.[16]

In the case of angle-resolved photoemission spectroscopy (ARPES), the beam spot of conventional systems is typically much larger than the size of the structural domains, and thus a superposition of the electronic structures from 90°-rotated domains is normally observed experimentally, doubling the number of observed bands and complicating the interpretation. While early measurements of such twinned samples suggested a reconstruction of the electronic structure below T_N,[17–21] a more detailed picture started to emerge with the first ARPES reports on detwinned samples of NaFeAs[22,23] and $BaFe_2As_2$.[24–26] Those results were influential in guiding the ideas of electronically driven nematicity,[4,5] and in particular it was claimed[22,23,25,27] that the detwinned results provided evidence for a large 50–80 meV energy scale associated with the splitting of bands with d_{xz} and d_{yz} orbital character which are degenerate in the tetragonal phase. However, recent studies of NaFeAs,[28] FeSe[29–31] and $BaFe_2As_2$[32] have questioned the existence of any large nematic energy scale. Moreover, the ARPES measurements on $BaFe_2As_2$ in the literature were never fully reconciled with the Fermi surface determined by quantum oscillations.[33] Meanwhile, alongside the general improvements in state-of-the-art ARPES systems and perfection of crystal growth techniques, a new opportunity is presented by the technical development of nano-ARPES, where the beam can

[1]Diamond Light Source, Harwell Campus, Didcot OX11 0DE, UK; [2]School of Physics and Astronomy, University of St. Andrews, St. Andrews KY16 9SS, UK; [3]Department of Physics, Royal Holloway, University of London, Egham, Surrey TW20 0EX, UK; [4]Laboratory for Quantum Magnetism, Institute of Physics, École Polytechnique Fédérale de Lausanne, CH-1015 Lausanne, Switzerland; [5]Graduate School of Science, Hiroshima University, Higashi-Hiroshima, Hiroshima 739-8526, Japan; [6]Leibniz Institute for Solid State and Materials Research, 01069 Dresden, Germany; [7]Institut für Festkörperphysik, Technische Universität Dresden, D-01171 Dresden, Germany and [8]DESY Photon Science, Deutsches Elektronen-Synchrotron, Hamburg, Germany
Correspondence: Matthew D. Watson (mdw5@st-andrews.ac.uk) or Timur K. Kim (timur.kim@diamond.ac.uk)

Received: 26 February 2019 Accepted: 19 June 2019
Published online: 16 July 2019

be focused to sub-micron areas, allowing the possibility of directly measuring ARPES in one domain – doing away with the necessity for straining the sample entirely. There is therefore a strong motivation to revisit the electronic structure of $BaFe_2As_2$ in one domain with ARPES.

In this paper we use high-resolution ARPES and nano-ARPES to find new insights into the electronic structure of the archetype parent compound $BaFe_2As_2$. We first present high-resolution measurements of a sample which was tuned from being twinned into an almost fully detwinned sample by the application of strain in situ. The electronic structure in one domain is found to match the 3D Fermi surface as determined by quantum oscillations. We reproduce a notable separation of bands along $\bar{\Gamma}-\bar{X}$ and $\bar{\Gamma}-\bar{Y}$ directions, previously interpreted in terms of a d_{xz}–d_{yz} orbital splitting. However, we argue that this energy scale should not be considered as a proxy for the energy scale of orbital ordering. Rather, our conclusion is that the electronic structure is strongly reconstructed across the whole bandwidth by the stripe AFM order. In addition, we used a nano-ARPES end station with a beam spot of <1 μm to directly measure ARPES spectra in one domain without requiring the application of any strain. These results show consistence with the high-resolution strained measurements, and allow us to use anisotropic features in the electronic structure to map the extensive stripe-like structural domains in real space.

RESULTS

The Fermi surface: theory and experiment

One of the most significant similarities between the cuprates and the Fe-based superconductors is that in both cases the parent compounds are antiferromagnetic, but a notable difference is that the parent compounds of Fe-based superconductors remain semimetallic[34] below T_N, albeit with a significantly reduced carrier density. A broad overview of the effects of this AFM order on the electronic structure of $BaFe_2As_2$, from the Density Functional Theory (DFT) perspective, is presented in Fig. 1a–d. When enforcing a non-magnetic solution, the calculation yields a compensated multiband Fermi surface in Fig. 1b, typical of Fe-based superconductors. This consists of three hole-like pockets at the centre of the Brillouin zone, and two electron-like pockets at the zone corner. In the ground state, however, the (π, 0, π) stripe AFM order of $BaFe_2As_2$ (Fig. 1a) doubles the size of the unit cell and maps the electron dispersions at the Brillouin zone corner back to the zone centre, where they hybridise strongly with the hole dispersions. However, the Fermi surface is not fully gapped, and the resulting Fermi surface in the magnetic phase can be qualitatively understood by considering three concepts. First, the size and shapes and of the pockets are not perfectly matched in the normal phase, particularly if one takes into account their warping along k_z, so the backfolding and hybridisation leaves behind small, typically 3D, pockets. Second, it has been shown that certain band hybridisations in the stripe AFM phase are forbidden exactly on the high-symmetry axes, enforcing a so-called "nodal SDW";[35] this leads to an expectation of tiny pockets with Dirac-like band dispersions localised on the high-symmetry axes.[18] Finally, charge compensation ensures that both hole- and electron-like pockets must contribute. These general considerations give a useful intuition into the form of the Fermi surface found in our antiferromagnetic DFT calculations shown in Fig. 1d, where the reconstructed Fermi surface of $BaFe_2As_2$ is found to consist of tiny 2D electron-like pockets centred in the $k_y = 0$ plane, and other small 3D hole- and electron-like pockets.

Turning now to the experimental determination of the electronic structure using ARPES, the overview Fermi surface map in Fig. 1e obtained at 150 K, above T_N, reveals a structure typical of non-magnetic Fe-based superconductors, with three hole pockets at the zone centre and two electron pockets at the Brillouin zone edge. Based on a combination of measurements in different geometries, our understanding is that all three hole pockets cross the Fermi level at 150 K, consistent with non-magnetic DFT and ref. [27] The measurements are strongly modulated by matrix elements effects,[36] but are qualitatively similar to the calculated Fermi surface, except that the sizes of the pockets are smaller than in the calculation,[32,37] and the features are broadened due to the elevated temperatures. However, at low temperatures, the overview Fermi surface on a twinned sample in Fig. 1f shows a completely different structure, prominently featuring four sharp bright spots around each high-symmetry point. These bright spots are in fact tiny electron-like Fermi surfaces, too small to be resolved in the measurement, and correspond to the tiny 2D tubes found in the DFT calculation. Notably, however, the calculation contains only two such tubes in the $\bar{\Gamma}-\bar{X}$ direction only, whereas four bright spots are observed experimentally due to the superposition of intensity from the two domains. This illustrates the necessity of extracting ARPES data from mono-domain samples to fully probe the intrinsic anisotropies of the electronic structure. In Fig. 1g, h we show overview Fermi surface maps measured on a sample under an applied strain; the data are taken on the same sample and in the same measurement geometry, but with the sample rotated by 90° (see Methods section). Here it is confirmed that, as in the calculations, in one domain there are only two bright spots, i.e. two tiny tube-like electron pockets. Moreover, the total absence of any spots in the other orientation, despite their intrinsic brightness in this geometry, indicates that this sample must be close to being 100% detwinned.

Much less brightly, one can also observe some faint intensity in replica bands, which are present with weak intensity in all measurements but are relatively more pronounced in Fig. 1g, where these replica states are marked by circles. This intensity cannot be ascribed to bulk electronic structure, but rather is a surface effect: after cleavage, the surface is terminated by Ba atoms, but not all atomic sites are occupied. This leads to possible surface reconstructions,[38] of which a $\sqrt{2}\times\sqrt{2}$ reconstruction seems to best account for our observations. However, importantly this intensity is weak, and localised away from the high-symmetry points of interest. We are thus confident in ascribing the principle intensity observed to bulk electronic structure, though a contribution from surface-derived states even on the high-symmetry axes is hard to fully exclude.[38,39]

A geometric detail of $BaFe_2As_2$ is that the body-centred symmetry of the unit cell imposes a screw symmetry along k_z at the corner of the Brillouin zone (Fig. 1a, b), similar to Sr_2RuO_4,[40] but notably different to the simpler primitive Brillouin zones of LiFeAs and FeSe. This adds complexity to the formal labelling of the Brillouin zone, which becomes further complicated by the stacking of the antiferromagnetic Brillouin zones (Fig. 1c). Since in experiments we always find a degree of k_z integration, in this paper we follow the convention of Yi et al.[25] to index our data in terms of a simplified effective surface Brillouin zone, using $\bar{X}, \bar{Y}$ to denote the corners of the non-magnetic Brillouin zone independent of k_z, and using $\bar{X}$ and $\bar{Y}$ separately for the a and b axes ($a > b$) in the case of data on detwinned samples.

Detailed Fermi surface structure in one domain

With this broad overview of the Fermi surface reconstruction in mind, we now turn to the high-resolution measurements in Fig. 2. In Fig. 2a, the sample was prepared on the detwinning rig, but the measurement was taken before any strain was deliberately applied. Some residual strain due to differential thermal expansion may have been present, but it seems to have been insufficient to significantly detwin the sample in this case. The data in Fig. 2a clearly contains contributions from both domain orientations, i.e., the sample was twinned. We then tuned the strain to induce a

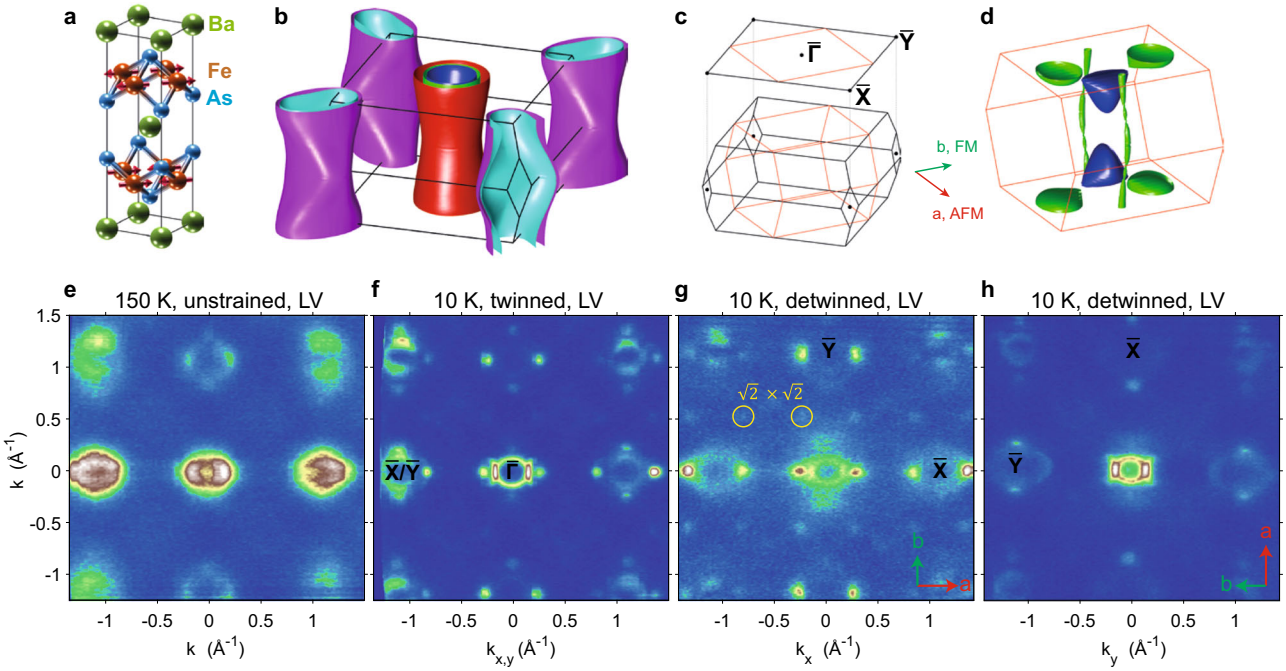

Fig. 1 Reconstructed Fermi surface in the AFM phase. **a** Crystal structure of $BaFe_2As_2$, in the high-temperature tetragonal *I*4/*mmm* space group. Arrows represent the orientation of magnetic moments on the Fe sites below T_N (fully described in the orthorhombic space group *Cccm*, not shown). **b** Calculated non-magnetic Fermi surface of $BaFe_2As_2$ in the tetragonal phase. **c** Geometry of the reconstruction of the Brillouin zone in the stripe AFM phase, and the definitions of the labels used in this paper, in an effective surface Brillouin zone. **d** Calculated Fermi surface in the reconstructed phase (blue = hole-like, green = electron-like). **e**–**h** Fermi surface maps obtained using 100 eV photons in Linear Vertical (LV) polarisation. Note that panel **h** is obtained on the same sample and with the same measurement geometry as **g**, only the sample is rotated 90° azimuthally. Panels **e**, **f** were obtained on a separate unstrained reference sample

transfiguration of the sample, from being fully twinned to being almost fully detwinned, entirely in situ. These detwinned measurements in Fig. 2b–g, taken in two orthogonal linear polarisations for completeness, allow the unmasking of the finer details of the Fermi surface in the AFM ground state.

According to the DFT calculation, the larger pockets are both predicted to be 3D, and centred at different k_z. At the chosen photon energy of 62 eV, the inner, almost circular hole band dominates the intensity in Fig. 2a. As the photon energy is linked to the k_z of the states probed in photoemission measurements, this indicates that the effective k_z here is tuned to an intermediate point bisecting the hole-like Fermi surface in Fig. 1d (see ref. [32] for detailed discussion of k_z-dependence in $BaFe_2As_2$). However, the fact that the outer taco-shaped electron-like band can be simultaneously observed in the measurements is already testament to the fact that there is a substantial degree of k_z-uncertainty in photoemission, due to both the finite escape depth of the photoelectron, and because the final state dispersions are in general unknown. Moreover, due to the variation of k_z with in-plane momentum, the measurements at $\bar{X}$ and $\bar{Y}$ probe k_z close to the $k_z = 0$ plane, and so only show the bright spots. Still, this geometry is convenient for relatively precise determinations of the in-plane shape of the Fermi surfaces, which are represented in the schematics in Fig. 2d, g.

The outlines of all the Fermi surfaces, especially the taco-shaped pockets, are seen most clearly in Fig. 2h, i, k where we present measurements at 25 eV photon energy. In Fig. 2h in particular, the highest resolution measurements in this paper, one can begin to see that the "bright spots" have an internal structure, and are in fact tiny electron-like pockets. The asymmetry of the spectral weight with respect to k_x in this geometry closely resembles the one-step photoemission calculations in ref. [41] and reflects a complex multiorbital character of the reconstructed Fermi surfaces. The k_z averaging effect results in the observation of mainly the outlines of extremal areas of the pockets, but also a continuum of spectral weight inside.

In order to make a more quantitative comparison to DFT calculations, in Fig. 2j we plot the Fermi surface obtained by collapsing the AFM DFT calculations over all k_z values. Although the observed Fermi surfaces in Fig. 2i, k are qualitatively similar to the calculation, the overall size of the Fermi pockets are significantly smaller than the DFT calculation shown in Fig. 2j, especially along k_y. It is well known that the Fermi surfaces of near-stoichiometric Fe-based superconductors in their tetragonal phases typically show smaller hole- and electron- pockets than predicted by DFT.[28,32,37,42,43] This applies to $BaFe_2As_2$ in the non-magnetic phase, since the observed Fermi surfaces in Fig. 1e are smaller than the corresponding calculation in Fig. 1b. The same effect persists in the magnetic phase, as the reconstructed Fermi surfaces in the AFM ground state are smaller than predicted by DFT.

Anisotropic band dispersions in the AFM phase

Having established the shape of the Fermi surface, we now turn to the electronic dispersions along the high-symmetry directions. The measurements on the twinned sample before applying strain in Fig. 3a are difficult to interpret, since the $\bar{\Gamma} - \bar{X}$ and $\bar{\Gamma} - \bar{Y}$ dispersions are observed simultaneously. After the strain is applied, however, the measurements on the now detwinned sample in Fig. 3b, c reveal the very distinct band dispersions along the $\bar{\Gamma} - \bar{X}$ and $\bar{\Gamma} - \bar{Y}$ directions at low temperatures.[24,25] Near $\bar{Y}$ in Fig. 3b, a relatively flat band is observed which remains fully occupied, whereas near $\bar{X}$ a band crosses the Fermi level in Fig. 3c, creating the tiny 2D tube-like Fermi surface pocket in combination with the an electron-like dispersion with d_{xy} character. This latter band is seen only in the opposite polarisation, labelled κ in Fig. 3e).[39] The lack of hybridisation between the two bands observed in opposite polarisations along $\bar{\Gamma} - \bar{X}$ is the origin of the 'Dirac'

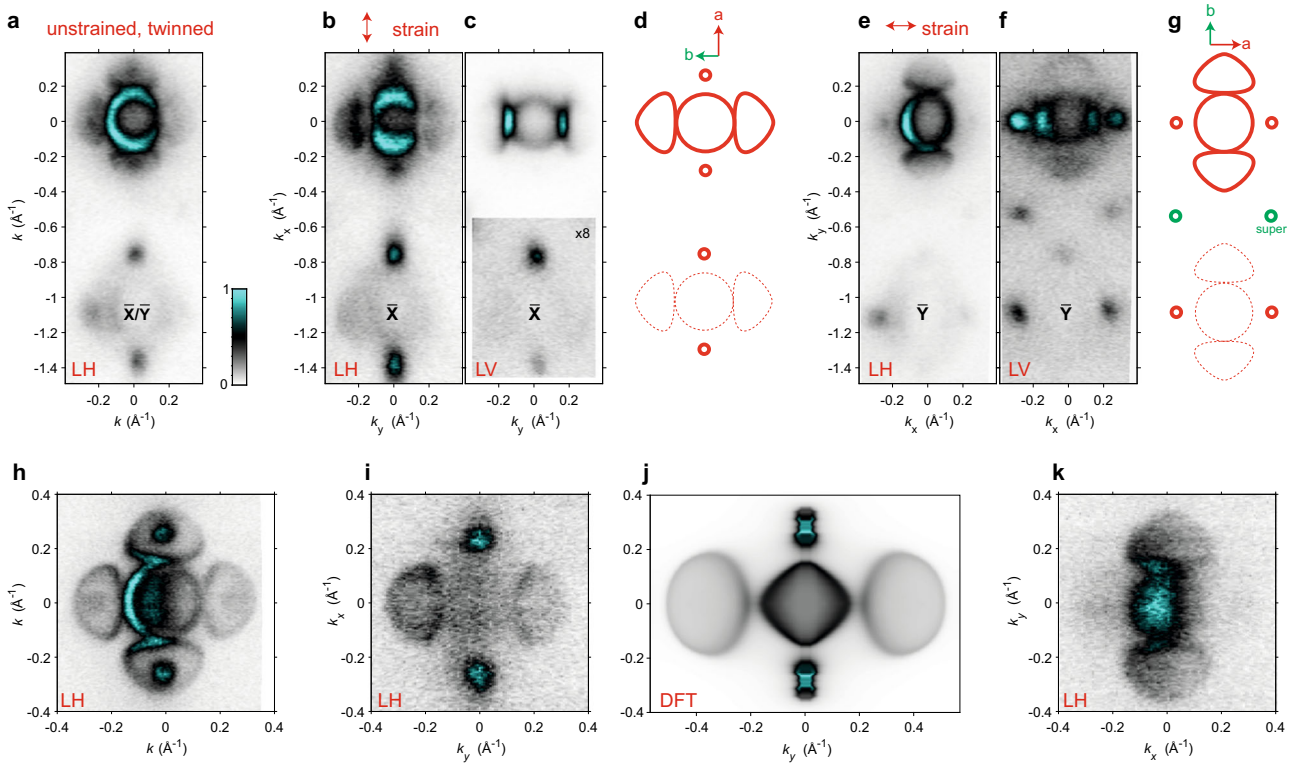

Fig. 2 Low-temperature Fermi surface maps before and after the application of strain. **a** Twinned Fermi surface, measured using 62 eV photons in LH polarisation before applying strain to the sample. **b**, **c** Fermi surfaces measured after straining (detwinning) in $\overline{\Gamma}-\overline{X}$ alignment in both LH and LV polarisations, and **d** schematic *in-plane* Fermi surfaces. **e**–**g** Equivalent for $\overline{\Gamma}-\overline{Y}$ alignment. Note that twinned data in **a** corresponds to a superposition of **b** and **e**. **h** Fermi surface map measured with 25 eV photons on a twinned sample. **i**, **k** Equivalent measurement on the detwinned samples in the two orientations, and **j** the k_z-collapsed Fermi surface calculated by DFT in the stripe AFM phase for comparison. All data measured at 7–10 K

character of the tiny electron-like Fermi surfaces. Focusing on a particular $k_{||}$ marked by the red arrows, we extract the Energy Distribution Curves (EDCs) shown in Fig. 3d. This analysis reveals a large 70 meV energy scale between the primary band dispersions in the two directions. It was previously proposed by Yi et al., that this large energy scale reflects an orbital ordering underlying the magnetic phase in the pure $BaFe_2As_2$, which was also observable independent of magnetic order in a $Ba(Fe_{0.975}Co_{0.025})_2As_2$ sample where T_s and T_N were split.[25] Very recently, Pfau et al. took this view a step further by trying to account for the low temperature dispersions by applying such an orbital ordering, and subsequently backfolding (but not hybridising) the dispersions.[27] However, here we take a contrasting view, by placing the AFM ordering in the driving seat.

From the DFT perspective, the stripe AFM of $BaFe_2As_2$ is not a weak-coupling SDW; that is to say, the low-temperature band dispersions cannot simply be accounted for by backfolding bands from the normal phase and weakly hybridising them. Rather, the magnetic order completely reconstructs the electronic structure, modifying the dispersions, orbital characters, and even the number of bands at low energies. For example, in the DFT calculation in Fig. 4f in the orthorhombic phase, there are three hole pockets at the Γ point. After backfolding the two electron dispersions, one might thus expect to find five states at low energies at the Γ point of the AFM phase; however, there is only one band found within 100 meV of the Fermi level at the Γ point in the AFM DFT calculation in Fig. 4e. The AFM thus completely reconstructs the band dispersions, with only a select few band dispersions surviving in a recognisable form (such as the d_{xy} dispersion at X in Fig. 4e). Moreover, as the $\Gamma-X$ and $\Gamma-Y$ directions correspond to AFM and FM spin alignments respectively, the band dispersions along $\Gamma-X$ and $\Gamma-Y$ will substantially differ in the AFM phase.

At first glance, the experimental dispersions in Fig. 4a, b do not appear to be so drastically reconstructed in the low temperature AFM phase, but in fact there are several signatures that point to a strong effect of the AFM order on the electronic structure. For instance, the states labelled χ in Fig. 4a, c, and ε in Fig. 3e are new states found only in the AFM phase, with no counterpart in the non-magnetic phase, but can be identified in the AFM calculation. The band labelled α in Fig. 4a was previously attributed to a shifted d_{yz} dispersion.[25,27] However, its appearance as an almost-symmetric V-shape along Γ-X cannot be reconciled with the much flatter dispersion of the d_{yz} band in Fig. 4d, f. Rather, a matching V-shaped dispersion is found in the AFM DFT calculations in Fig. 4c, e, which is qualitatively distinct from any dispersion in the non-magnetic phase. We already showed that the Fermi surface is in qualitative agreement with the DFT prediction, but it is worth emphasising that, if one were to simply backfold the non-magnetic bands, one would inevitably find several more small pockets than are actually found. The comparison between the DFT and experiment requires some careful thought, as some band shifts are required. Moreover, not all the eigenvalues in the AFM calculation will give significant spectral weight in ARPES, and the k_z integration is always relevant to the observations. However, overall we can make enough one to one correspondences in Fig. 4a, c that we can be satisfied that, broadly speaking, the DFT perspective is correct: the AFM ordering strongly reconstructs the electronic structure, across the whole bandwidth, and dominates over any orbital or nematic ordering.

Returning to the ~70 meV energy scale as originally found by Yi et al.,[25] the corresponding bands are identified by circles in the

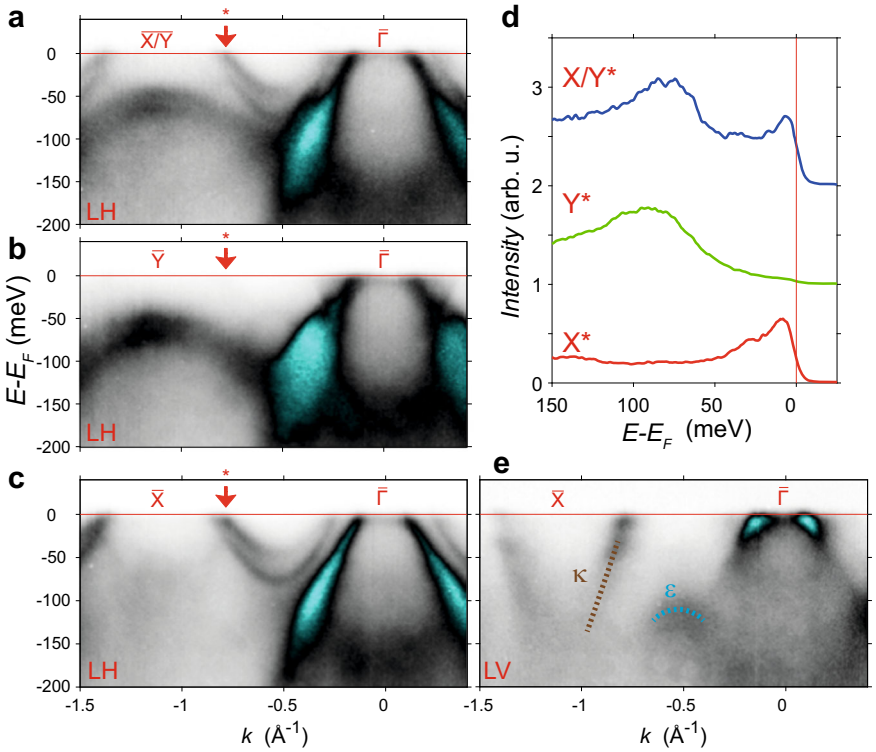

Fig. 3 Distinct band dispersions along $\bar{\Gamma}-\bar{X}$ and $\bar{\Gamma}-\bar{Y}$. **a** High-symmetry dispersion before applying strain and **b**, **c** equivalent measurements on the same sample after straining, which is now in a detwinned state, with the sample oriented along $\bar{\Gamma}-\bar{Y}$ and $\bar{\Gamma}-\bar{X}$ respectively. The difference between the two orientations is particularly prominent at the *k*-point labelled by the starred arrow, from which the EDCs in **d** are extracted, showing an apparent ~70 meV energy scale. **e** Measurement with equivalent geometry to **c** but with LV light polarisation, which highlights other states including a band (*κ*) with mainly d_{xy} character. The states labelled *κ* and *ε* are also marked in Fig. 4c and referred to in the main text. All measurements performed using $h\nu = 62$ eV at 7–10 K

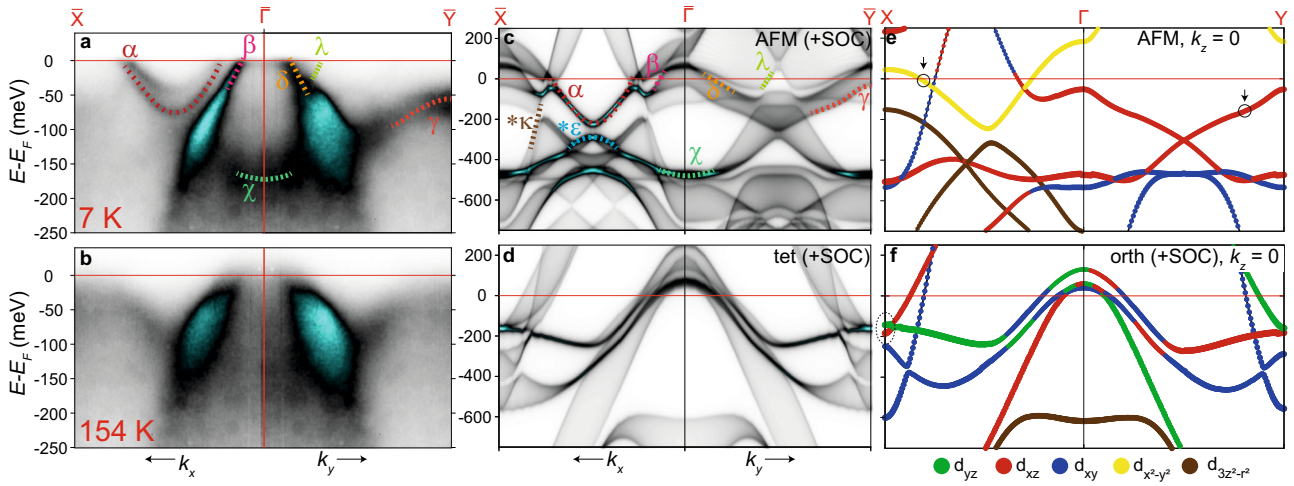

Fig. 4 Comparisons of data above and below T_N with DFT. **a** Stitched ARPES measurements along the orthogonal high-symmetry axes (same data as Fig. 3b, c) and **b** equivalent measurements above T_N. **c** DFT calculation in the AFM ground state, with band dispersions averaged along the k_z axis to generate a spectral function. Note that in the experiments, the intensities are very different, since not all eigenvalues will have equal spectral weight in the magnetic phase, and also there are severe matrix element effects. Nevertheless, good correspondence can be seen for certain states, as labelled. Note that the starred states, labelled *ε* and *κ*, are found in LV polarisation in Fig. 3e. **d** Equivalent projection of DFT calculations in the tetragonal phase. **e** Calculated dispersion at $k_z = 0$ only in the AFM phase, with orbital characters shown. Small circles note the bands which mainly contribute to the EDCs shown in Fig. 3d. **f** Calculated dispersions at $k_z = 0$ in the orthorhombic phase. The orthorhombicity lowers the d_{xz}/d_{yz} degeneracy, especially noticeable at *X* as highlighted by the dashed ellipse

DFT calculation in Fig. 4e, which suggests that the lower band, found near $\bar{Y}$, is likely to have d_{xz} orbital character, but the upper dispersion $\bar{X}$ is predicted to have mainly $d_{x^2-y^2}$ character and only minority d_{yz} character. Thus we argue that it is not possible to cleanly ascribe this energy scale as being due to "orbital ordering" lifting the degeneracy of d_{xz} and d_{yz} states, firstly, because the orbital content changes (at least, in this DFT calculation), secondly, because it is only applicable to a particular $k_{||}$ and our data is not

generally suggestive of a persistent orbital polarisations at other points and thirdly, because all of the changes in the band structure are inseparable from the dominant effect of the magnetic ordering. Furthermore, our temperature-dependent data (shown in supplementary information, SI) demonstrates that the majority of the band structure changes occur relatively abruptly at $T_s = T_N = 137$ K. This is in line with the observation of a first-order phase transition in thermodynamic measurements.[44] However, since the transition is first order, the procedure of tracking bands from the non-magnetic phase into the ordered phase[25,27] is questionable in $BaFe_2As_2$, especially given the high scattering rate at temperatures around T_N.

Of course, there is a significant discrepancy between the energy scales of the data and the DFT calculations. The experiments show an overall renormalisation of the bandwidth of a factor of ~3,[24] in both the non-magnetic and ordered phases, which is usually attributed to strong on-site electron correlations. Dynamical Mean Field Theory (DMFT) has been a widely used tool to treat the strong local Hund's and Coulomb terms within the Fe 3*d* orbitals, overcoming the limitations of DFT in describing such interactions and achieving much better correspondence with experiments on the overall energy scales of the dispersions.[45,46] Although relatively few studies have treated the AFM phase within DMFT or similar techniques, our data appear to be well matched in terms of overall energy scales and anisotropies with the magnetic DMFT calculation of Yin et al.[47] However, we find that other than the overall bandwidth renormalisation, DFT in the stripe AFM phase offers a good description of the band dispersions, as is evidenced by the agreement between calculated and measured Fermi surfaces in Fig. 3.

nano-ARPES: band dispersions from within individual domains

Until recently, the only method of directly accessing the underlying anisotropies in the electronic structure of antiferromagnetic parent compounds has been the application of an external strain, as we have used above. However, the external strain will smear out the phase transition as the symmetry is already broken, and due to magnetoelastic coupling the strain could even lead to the stabilisation of new phases, as found in LiFeAs.[48] Moreover, the combination of strain with ARPES gives several challenges related to possible bending and cracking of the sample surface, and strain inhomogeneity. In the following, we take a new approach: instead of creating effective macroscopic mono-domain samples by applying strain so that it is suitable for traditional ARPES, we use the tightly focused beam of a nano-ARPES system to direct measure photoemission from within single antiferromagnetic domains in an unstrained sample.

Previous studies of domain formation in $BaFe_2As_2$ have shown that in unstrained samples, domains typically form as long stripes, with straight boundaries separated by a characteristic spacing of a few microns.[12,14,49] This inevitably means that a superposition of intensity from two domains is detected in a traditional ARPES set-up, with a typical beam spot of 50 µm or larger (Fig. 5a). Developments in laser-ARPES have reduced the spot size to a few microns,[50] and in a recent study Schwier et al. were able to visualise some spatial variation of the intensities of hole pocket dispersions near the Γ point in FeSe, which was associated with domain structures.[51] However, the capability to combine excellent spatial resolution and full *k*-space mapping has become recently accessible to state-of-the-art nano-ARPES, where the beam spot can be focused to better than 700 nm in diameter. The greatly decreased spot size in our nano-ARPES apparatus comes at the price of a substantially lower count rate, necessitating measurements with lower energy resolution, and also a lower signal/noise ratio. Nevertheless, it provides an excellent opportunity to study electronic anisotropies in a strain-free measurement, resolving any questions over the influence of the external strain in the traditional ARPES measurements.

Our chosen measurement geometry probes a dispersion through the $\overline{X}, \overline{Y}$ points at 70 eV in LH polarisation. Due to the selection rules in this geometry, each domain mainly contributes just one band: as can be seen in our traditional ARPES reference data in Fig. 5f, the band from one domain approaches the Fermi level to create the tiny spot-like pockets; in the other domain, a band is observed at higher binding energies (with correspondingly higher linewidth due to electron–electron scattering), reaching a maximum ~100 meV below E_F at the high-symmetry point, where the intensity also vanishes.

As these two bands are well-separated in both energy and momentum, they function as convenient indicators of the contribution of each domain, at any given spot on the sample. They are roughly equivalent in total intensity, so the spatial map of the integrated intensity in Fig. 5c is largely uniform, showing no clear domain-like structures. However, the underlying domain structure is revealed in Fig. 5d, where the colour scale is proportional to the intensity of a region of interest corresponding to the upper dispersion (R1 in Fig. 5g. This reveals straight, parallel domains, with a lateral spacing of ~2 µm, consistent with the structures observed in the literature.[12,14,49] The upper part of the spatial map includes a probable crack or defect in the sample, also visible in the total counts in Fig. 5c. This feature seems to locally pin a particular domain, presumably due to some residual stress. However, the main domains appear to run straight through this. We may speculate that a crack or terrace-like feature may be present only at the surface, while the main domains presumably extend vertically deep into the sample. An important test is that the domain contrast should flip when analysing the spatial map for the lower R2 regions of interest. This is confirmed in Fig. 5e, where the intensity pattern is reversed compared with Fig. 5d.

This analysis allows us to precisely position the beam spot inside either domain, allowing for the unprecedented collection of band dispersions from within a single domain (see SI for spectra obtained at a fixed light spot). Alternatively, one can build up a mono-domain spectrum by summing intensity from pixels in the spatial map which have the highest contrast for the desired domain; the results of this filtering technique are shown in Fig. 5g, h, which indeed reveals "detwinned-like" dispersions. This filtering technique generates effective mono-domain dispersions, while overcoming the experimental challenges of sample drift and degradation.

From a technical perspective, these nano-ARPES results push the boundaries of achieving detailed band structure information from within micron-size domains. Our results are very promising for further nano-ARPES studies of other quantum materials which exhibit magnetic or structural domains in their ground states, allowing the spatial mapping of electronic anisotropies. The combination of spatial and momentum resolutions demonstrated in this paper is also beginning to find more widespread applications to systems where approximate micron length scales are relevant, such as in the study of crystals where cleavage yields multiple surface terminations[52–54] or only small regions with flat surfaces,[55,56] systems exhibiting phase separation, and patterned devices. We hope that the data presented above can therefore serve as a proof-of-concept study on a material which is well known to the quantum materials community, to motivate further use of this technique.

Beyond the technical achievement, however, there are two important scientific points. Firstly, our nano-ARPES results are consistent with the traditional ARPES measurements on detwinned samples: we have shown that the bands forming the bright spots in the Fermi surface derive from different domains, with each domain giving just two bright spots (tiny electron pockets). Thus, we can lay to rest any worry that the ARPES measurement on detwinned samples are unduly influenced by the

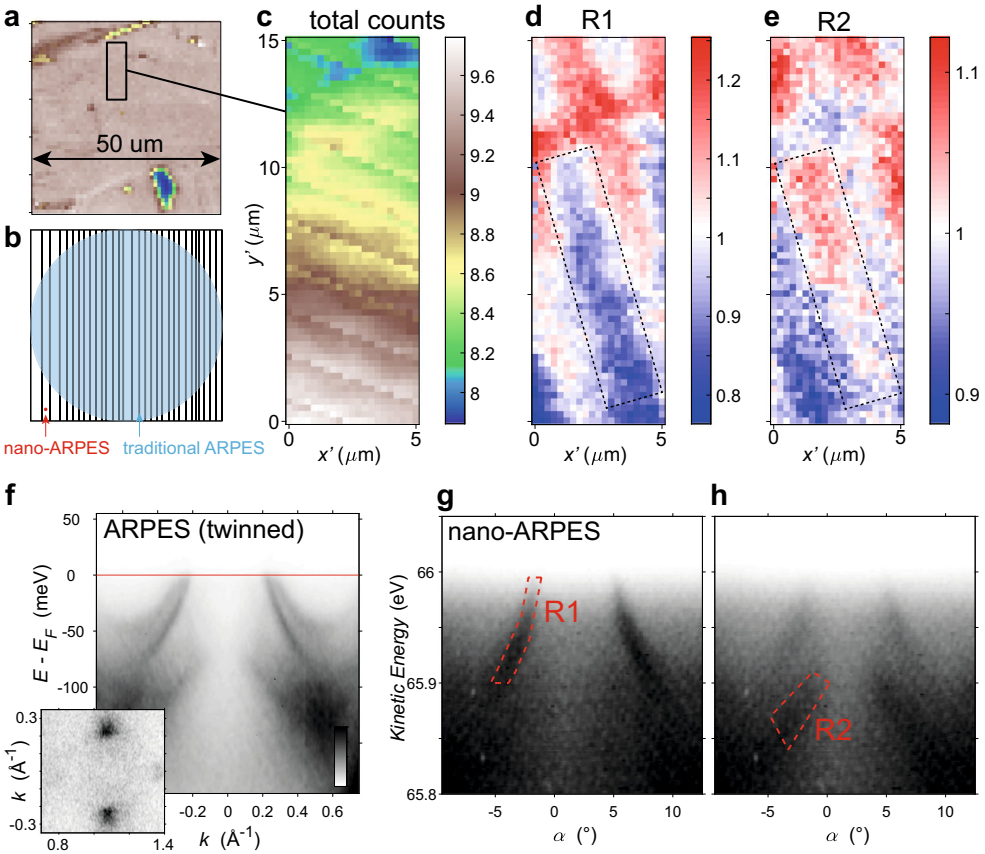

Fig. 5 Mapping of real space and reciprocal space structures with nano-ARPES. **a** Total intensity map over a 50-μm region, from which a 5 × 15 μm area was selected for detailed study. **b** Illustration of the relative beam size of nano-ARPES versus conventional ARPES. Vertical lines represent typical domain sizes in $BaFe_2As_2$. **c** Total intensity map of the detailed area, which is largely featureless (the stripes in this image are artefacts caused by the periodic "top-ups" of the synchrotron, which weakly modulates the incident flux). Note that the x', y' spatial axes here are rotated with respect to the crystallographic axes. The hidden domain structures are revealed by analysing the intensity within **d** region of interest R1 and **e** region of interest R2 (normalised by the total count at each pixel). Dotted black line is a guide to see the reversal of the domain pattern. **f** Reference measurements obtained with traditional ARPES on a twinned sample, inset showing the Fermi surface. **g**, **h** Effective single-domain spectra, extracted from a filtering technique, summing intensity at the pixels with the top (**g**) and bottom (**h**) 10% contrast of region R1. Note that for practical purposes, the spatial mapping data is analysed using the raw, not *k*-scaled data; we therefore choose to plot the raw data here. The offset in angle, α, arises from a slight tilt of the sample from imperfect mounting. Note that the regions of interest are defined including a symmetric area at positive angles, which is not shown. All nano-ARPES data measured at 25 K

application of the external strain, and confirm that the ARPES data here and in the literature on detwinned samples can indeed be safely interpreted as the intrinsic spectral function of one domain (for a fully detwinned sample). Secondly, our measurements act as a reminder that, within the 50 μm beam spot on a nominally clean single crystal, there can be several cracks, inclusions, inhomogeneities, as well as domain structures, which are all integrated into the traditional ARPES measurement. Such microscopic information, on a length scale which spans the regimes of STM and traditional ARPES, is important for interpretation of the spectroscopy data obtained with a macroscopic beam spot.

DISCUSSION

The Fermi surface we have measured closely resembles that deduced by quantum oscillations.[33] Moreover, the small pockets of compensated carriers, including a small number of highly mobile carriers from the quasi-2D tube-like electron pockets with Dirac-like dispersions, would also provide a consistent explanation of the magnetotransport data.[57] Although the DFT prediction differs from this in terms of the size of the pockets, the topology of the band is found to be consistent. Our study also resolves several inconsistencies in the previous ARPES data: Yi et al.[25] indicated several more Fermi surfaces than were detected by quantum oscillations or predicted by DFT, while other previous studies also lacked the resolution to be precise on the nature of the Fermi surface.[18,19,24,39] Only very recently, Fedorov et al.[32] reported Fermi surfaces measured on twinned samples that, for the first time, appeared broadly consistent with DFT calculations on $BaFe_2As_2$. Here, with high-resolution measurements on detwinned samples, we cement the experimental Fermi surface of $BaFe_2As_2$ in one domain, and reveal how the magnetic ordering anisotropically reconstructs the electronic structure over the whole bandwidth.

In another very recent study, Pfau et al. described the ground state dispersions of $BaFe_2As_2$ by applying band shifts which they associated with nematic order, and then backfolded the bands, i.e., giving prominence to the orbital ordering due to its apparently large energy scale and taking a weak-coupling approach to the AFM.[27] Our ab-initio-based approach gives us the opposite philosophy: we argue that the AFM severely reconstructs the electronic structure over the whole bandwidth, and magnetism is firmly in the driving seat. The low temperature Fermi surface provides strong support for our approach, since it is nearly correct in the AFM DFT calculation, but any simple backfolding procedure would lead to far more pockets than are actually observed.[27] However, we note that the scenario is somewhat different in NaFeAs, where due to the much lower T_N

and much weaker ordered moment (0.09 μ_B rather than 0.87 μ_B in $BaFe_2As_2$[58]), the magnetic ordering is more SDW-like and the approach of understanding the ground state Fermi surface in terms of backfolded bands is more fruitful.[28] The presence of two tiny tube-like Fermi pockets, appearing as two bright spots along the $\bar{\Gamma} - \bar{X}$ direction in the measurements, gives a strongly unidirectional character to the measured Fermi surface of $BaFe_2As_2$, and is reminiscent of the as-yet unexplained observation of only the electron pocket oriented along the *a* axis in detwinned measurements of the nematic phase of FeSe.[30] We speculate that there is indeed a connection between the two observations, but we leave this to future work to unravel.

In conclusion, we have used high-resolution ARPES measurements of detwinned $BaFe_2As_2$ to revisit the ground electronic state in the magnetically ordered phase. We have shown that the Fermi surface in the AFM phase includes both 3D pockets and tiny quasi-2D tubes, closely matching the prediction of DFT in the AFM phase, though with smaller in-plane size. The observed low temperature dispersions cannot be understand by simply shifting and backfolding the high-temperature dispersions, but rather the magnetic order reconstructs the electronic structure over the whole bandwidth. Our measurements of samples detwinned by the application of a mechanical strain were corroborated by nano-ARPES measurements, in which the spot scanned over individual domains and single-domain spectra were obtained on an unstrained sample. Overall, the revision of the ARPES evidence presented here puts the spotlight back onto magnetic interactions as the main ingredient in the phase diagrams based on $BaFe_2As_2$, the archetypal parent compound of Fe-based superconductors.

METHODS

High quality single crystals of $BaFe_2As_2$ were grown by the self flux technique.[59] For the detwinned measurements, a sample with approximate dimensions of $1500 \times 1200 \times 50$ µm with uniform thickness and regular facets was selected and mounted across the plates of the horseshoe-shaped device, aligned by eye (within ~2°) such that the Fe–Fe direction was parallel with the direction of strain. Silver epoxy (Epo-Tek H27D) was used to mount the sample and also acted as a medium to transmit the strain into the sample. Due to the finite Poisson's ratio, the actual strain on the sample ought to be described by a full strain tensor, but for simplicity we refer to a unidirectional tensile strain. The photoelectron energy and angular distributions were analysed with a SCIENTA R4000 hemispherical analyser The angular resolution was 0.2°, and the overall energy resolution was better than 10 meV. Nano-ARPES measurements were performed on a similar sample using 70 eV photon energy and SCIENTA DA30 analyser, at a temperature of 30 K and with a typical energy resolution of ≈30 meV chosen due to the much lower count rate, and angular resolution of ~0.2°. It was found that prolonged exposure (>30 min) of the sample to the focused beam spot at a fixed position caused local sample degradation, but in scanning mode (typically 1 min/pixel) this was not a serious problem. Both ARPES and nano-ARPES measurements were performed at the I05 beamline at the Diamond Light Source, UK.[60] The density functional theory (DFT) calculations were performed using the Wien2k code, as detailed in the SI.

DATA AVAILABILITY

The datasets analysed during the current study are available from the corresponding authors upon reasonable request.

ACKNOWLEDGEMENTS

We thank S. Backes, S. V. Borisenko, N. B. M. Schröter, M. Eschrig, R. Valenti and C. Cacho for useful discussions. We thank Diamond Light Source for access to beamline I05 (proposal numbers SI15074, SI19041) that contributed to the results presented here. The work at IFW was supported by the Deutsche Forschungsgemeinschaft (DFG) through the Priority Programme SPP1458. L.C.R. is supported by an iCASE studentship of the UK Engineering and Physical Sciences Research Council (EPSRC) and Diamond Light Source Ltd CASE award. S.A. thanks the DFG for funding (AS 523/4-1 & 523/3-1).

AUTHOR CONTRIBUTIONS

ARPES experiments were performed by M.D.W., L.C.R., H.I. and T.K.K. Nano-ARPES experiments were performed by M.D.W., P.D., L.C.R., D.V.E., H.I. and T.K.K. The acquisition of both data sets was enabled by innovations at the I05 beamline developed by P.D., H.I., M.D.W., T.K.K. and M.H. Samples were grown by S.A., S.W. and B.B.; M.D.W. analysed the data, performed the DFT calculations and wrote the manuscript with T.K.K., with input from all co-authors. The overall project was led by M.D.W. and T.K.K.

ADDITIONAL INFORMATION

Supplementary information accompanies the paper on the *npj Quantum Materials* website (https://doi.org/10.1038/s41535-019-0174-z).

Competing interests: The authors declare no competing interests.

Publisher's note: Springer Nature remains neutral with regard to jurisdictional claims in published maps and institutional affiliations.

REFERENCES

1. Nandi, S. et al. Anomalous suppression of the orthorhombic lattice distortion in superconducting $Ba(Fe_{1-x}Co_x)_2As_2$ single crystals. *Phys. Rev. Lett.* **104**, 057006 (2010).
2. Wright, J. D. et al. Gradual destruction of magnetism in the superconducting family $NaFe_{1-x}Co_xAs$. *Phys. Rev. B* **85**, 054503 (2012).
3. Böhmer, A. E. & Kreisel, A. Nematicity, magnetism and superconductivity in FeSe. *J. Phys. Condens. Matter* **30**, 023001 (2017).
4. Fernandes, R. M., Chubukov, A. V. & Schmalian, J. What drives nematic order in iron-based superconductors? *Nat. Phys.* **10**, 97 (2014).
5. Yi, M., Zhang, Y., Shen, Z.-X. & Lu, D. Role of the orbital degree of freedom in iron-based superconductors. *npj Quant. Mater.* **2**, 57 (2017).
6. Fernandes, R. M., Chubukov, A. V., Knolle, J., Eremin, I. & Schmalian, J. Preemptive nematic order, pseudogap, and orbital order in the iron pnictides. *Phys. Rev. B* **85**, 024534 (2012).
7. Wysocki, A. L., Belashchenko, K. D. & Antropov, V. P. Consistent model of magnetism in ferropnictides. *Nat. Phys.* **7**, 485 (2011).
8. Glasbrenner, J. K. et al. Effect of magnetic frustration on nematicity and superconductivity in iron chalcogenides. *Nat. Phys.* **11**, 953 (2015).
9. Baek, S.-H. et al. Orbital-driven nematicity in FeSe. *Nat. Mater.* **14**, 210 (2014).
10. Yamakawa, Y., Onari, S. & Kontani, H. Nematicity and magnetism in FeSe and other families of Fe-Based superconductors. *Phys. Rev. X* **6**, 021032 (2016).
11. Kissikov, T. et al. Uniaxial strain control of spin-polarization in multicomponent nematic order of $BaFe_2As_2$. *Nat. Commun.* **9**, 1058 (2018).
12. Tanatar, M. A. et al. Uniaxial-strain mechanical detwinning of $CaFe_2As_2$ and $BaFe_2As_2$ crystals: optical and transport study. *Phys. Rev. B* **81**, 184508 (2010).
13. Chu, J.-H. et al. In-plane resistivity anisotropy in an underdoped iron arsenide superconductor. *Science* **329**, 824–826 (2010).
14. Fisher, I. R., Degiorgi, L. & Shen, Z. X. In-plane electronic anisotropy of underdoped '122' Fe-arsenide superconductors revealed by measurements of detwinned single crystals. *Rep. Prog. Phys.* **74**, 124506 (2011).
15. Baum, A. et al. Interplay of lattice, electronic, and spin degrees of freedom in detwinned $BaFe_2As_2$: a Raman scattering study. *Phys. Rev. B* **98**, 075113 (2018).
16. Lu, X. et al. Spin waves in detwinned $BaFe_2As_2$. *Phys. Rev. Lett.* **121**, 067002 (2018).
17. Zabolotnyy, V. B. et al. (π, π) electronic order in iron arsenide superconductors. *Nature* **457**, 569 (2009).
18. Richard, P. et al. Observation of dirac cone electronic dispersion in $BaFe_2As_2$. *Phys. Rev. Lett.* **104**, 137001 (2010).
19. Shimojima, T. et al. Orbital-dependent modifications of electronic structure across the magnetostructural transition in $BaFe_2As_2$. *Phys. Rev. Lett.* **104**, 057002 (2010).
20. de Jong, S. et al. Droplet-like Fermi surfaces in the anti-ferromagnetic phase of $EuFe_2As_2$, an Fe-pnictide superconductor parent compound. *EPL Europhys. Lett.* **89**, 27007 (2010).
21. Wang, Q. et al. Symmetry-broken electronic structure and uniaxial Fermi surface nesting of untwinned $CaFe_2As_2$. *Phys. Rev. B* **88**, 235125 (2013).
22. Yi, M. et al. Electronic reconstruction through the structural and magnetic transitions in detwinned NaFeAs. *New J. Phys.* **14**, 073019 (2012).
23. Zhang, Y. et al. Symmetry breaking via orbital-dependent reconstruction of electronic structure in detwinned NaFeAs. *Phys. Rev. B* **85**, 085121 (2012).
24. Kim, Y. et al. Electronic structure of detwinned $BaFe_2As_2$ from photoemission and first principles. *Phys. Rev. B* **83**, 064509 (2011).
25. Yi, M. et al. Symmetry-breaking orbital anisotropy observed for detwinned $Ba(Fe_{1-x}Co_x)_2As_2$ above the spin density wave transition. *Proc. Natl Acad. Sci. USA* **108**, 6878–6883 (2011).

26. Sonobe, T. et al. Orbital-anisotropic electronic structure in the nonmagnetic state of $BaFe_2(As_{1-x}P_x)_2$ superconductors. *Sci. Rep.* **8**, 2169 (2018).
27. Pfau, H. et al. Detailed band structure of twinned and detwinned $BaFe_2As_2$ studied with angle-resolved photoemission spectroscopy. *Phys. Rev. B* **99**, 035118 (2019).
28. Watson, M. D. et al. Three-dimensional electronic structure of the nematic and antiferromagnetic phases of NaFeAs from detwinned angle-resolved photoemission spectroscopy. *Phys. Rev. B* **97**, 035134 (2018).
29. Watson, M. D. et al. Evidence for unidirectional nematic bond ordering in FeSe. *Phys. Rev. B* **94**, 201107 (2016).
30. Watson, M. D., Haghighirad, A. A., Rhodes, L. C., Hoesch, M. & Kim, T. K. Electronic anisotropies revealed by detwinned angle-resolved photo-emission spectroscopy measurements of FeSe. *New J. Phys.* **19**, 103021 (2017).
31. Fedorov, A. et al. Effect of nematic ordering on electronic structure of FeSe. *Sci. Rep.* **6**, 36834 (2016).
32. Fedorov, A. et al. Energy scale of nematic ordering in the parent iron-based superconductor: $BaFe_2As_2$. *arXiv:1811.02430* (2018).
33. Terashima, T. et al. Complete fermi surface in $BaFe_2As_2$ observed via shubnikov–de haas oscillation measurements on detwinned single crystals. *Phys. Rev. Lett.* **107**, 176402 (2011).
34. Mazin, I. I. Superconductivity gets an iron boost. *Nature* **464**, 183 (2010).
35. Ran, Y., Wang, F., Zhai, H., Vishwanath, A. & Lee, D.-H. Nodal spin density wave and band topology of the feas-based materials. *Phys. Rev. B* **79**, 014505 (2009).
36. Brouet, V. et al. Impact of the two Fe unit cell on the electronic structure measured by ARPES in iron pnictides. *Phys. Rev. B* **86**, 075123 (2012).
37. Borisenko, S. V. et al. Direct observation of spin-orbit coupling in iron-based superconductors. *Nat. Phys.* **12**, 311 (2015).
38. van Heumen, E. et al. Existence, character, and origin of surface-related bands in the high temperature iron pnictide superconductor $BaFe_{2-x}Co_xAs_2$. *Phys. Rev. Lett.* **106**, 027002 (2011).
39. Fuglsang Jensen, M. et al. Angle-resolved photoemission study of the role of nesting and orbital orderings in the antiferromagnetic phase of $BaFe_2As_2$. *Phys. Rev. B* **84**, 014509 (2011).
40. Bergemann, C., Mackenzie, A. P., Julian, S. R., Forsythe, D. & Ohmichi, E. Quasi-two-dimensional Fermi liquid properties of the unconventional superconductor Sr_2RuO_4. *Adv. Phys.* **52**, 639–725 (2003).
41. Derondeau, G., Braun, J., Ebert, H. & Minár, J. Theoretical study on the anisotropic electronic structure of antiferromagnetic $BaFe_2As_2$ and Co-doped $Ba(Fe_{1-x}Co_x)_2As_2$ as seen by angle-resolved photoemission. *Phys. Rev. B* **93**, 144513 (2016).
42. Ortenzi, L., Cappelluti, E., Benfatto, L. & Pietronero, L. Fermi-surface shrinking and interband coupling in iron-based pnictides. *Phys. Rev. Lett.* **103**, 046404 (2009).
43. Carrington, A. Quantum oscillation studies of the fermi surface of iron-pnictide superconductors. *Rep. Prog. Phys.* **74**, 124507 (2011).
44. Böhmer, A. E. et al. Superconductivity-induced re-entrance of the orthorhombic distortion in $Ba_{1-x}K_xFe_2As_2$. *Nat. Commun.* **6**, 7911 (2015).
45. Watson, M. D. et al. Formation of Hubbard-like bands as a fingerprint of strong electron-electron interactions in FeSe. *Phys. Rev. B* **95**, 081106 (2017).
46. Evtushinsky, D. V. et al. High-energy electronic interaction in the 3*d* band of high-temperature iron-based superconductors. *Phys. Rev. B* **96**, 060501 (2017).
47. Yin, Z. P., Haule, K. & Kotliar, G. Magnetism and charge dynamics in iron pnictides. *Nat. Phys.* **7**, 294 (2011).
48. Yim, C. M. et al. Discovery of a strain-stabilised smectic electronic order in lifeas. *Nat. Commun.* **9**, 2602 (2018).
49. Kirtley, J. R., Kalisky, B., Luan, L. & Moler, K. A. Meissner response of a bulk superconductor with an embedded sheet of reduced penetration depth. *Phys. Rev. B* **81**, 184514 (2010).
50. Iwasawa, H. et al. Development of laser-based scanning μ-ARPES system with ultimate energy and momentum resolutions. *Ultramicroscopy* **182**, 85–91 (2017).
51. Schwier, E. F. et al. Applications for ultimate spatial resolution in laser based -ARPES: a fese case study. *AIP Conf. Proc.* **2054**, 040017 (2019).
52. Noguchi, R. et al. A weak topological insulator state in quasi-one-dimensional bismuth iodide. *Nature* **566**, 518–522 (2019).
53. Mazzola, F. et al. Itinerant ferromagnetism of the Pd-terminated polar surface of $PdCoO_2$. *Proc. Natl Acad. Sci. USA* **115**, 12956–12960 (2018).
54. Iwasawa, H. et al. Buried double CuO chains in $YBa_2Cu_4O_8$ uncovered by nano-ARPES. *Phys. Rev. B* **99**, 140510 (2019).
55. Schröter, N. B. M. et al. Chiral topological semimetal with multifold band crossings and long Fermi arcs. *Nat. Phys.* (2019).
56. Valbuena, M. A. et al. Polarization dependence of angle-resolved photoemission with submicron spatial resolution reveals emerging one-dimensionality of electrons in $NbSe_3$. *Phys. Rev. B* **99**, 075118 (2019).
57. Ishida, S. et al. Manifestations of multiple-carrier charge transport in the magnetostructurally ordered phase of $BaFe_2As_2$. *Phys. Rev. B* **84**, 184514 (2011).
58. Dai, P. Antiferromagnetic order and spin dynamics in iron-based superconductors. *Rev. Mod. Phys.* **87**, 855–896 (2015).
59. Aswartham, S. et al. Single crystal growth and physical properties of superconducting ferro-pnictides $Ba(Fe, Co)_2As_2$ grown using self-flux and Bridgman techniques. *J. Cryst. Growth* **314**, 341–348 (2011).
60. Hoesch, M. et al. A facility for the analysis of the electronic structures of solids and their surfaces by synchrotron radiation photoelectron spectroscopy. *Rev. Sci. Instrum.* **88**, 013106 (2017).